**A&A manuscript no.**
(will be inserted by hand later)

**Your thesaurus codes are:**
**06(08.14.2, 08.13.1, 08.09.2 RX J1313.2–3259, 08.02.1, 13.25.5 ,02.01.2)**

ASTRONOMY
AND
ASTROPHYSICS

# RX J1313.2–3259, a long-period Polar discovered with ROSAT ⋆

**H.-C. Thomas**[1], **K. Beuermann**[2,3], **V. Burwitz**[3,2], **K. Reinsch**[2], and **A.D. Schwope**[4],

[1] MPI für Astrophysik, Karl-Schwarzschild-Str. 1, D-85740 Garching, Germany
[2] Universitäts-Sternwarte, Geismarlandstr. 11, D-37083 Göttingen, Germany
[3] MPI für extraterrestrische Physik, Giessenbachstr. 6, D-85740 Garching, Germany
[4] Astrophysikalisches Institut Potsdam, An der Sternwarte 16, D-14482 Potsdam, Germany

Received 7 September 1999 / Accepted 5 November 1999

**Abstract.** We report observations of a new AM Herculis binary identified as the optical counterpart of the X-ray source RX J1313.2–3259, detected during the ROSAT All-Sky Survey (RASS). It has an orbital period of 251 min and is strongly modulated at optical wavelengths. The long-term behavior is characterized by a pronounced variation in X-rays between the RASS and two subsequent pointings (decrease by a factor 40 in count rate) and by moderate changes in the optical brightness (up to a factor 5). The X-ray spectrum is dominated by a soft quasi-blackbody component, with a smaller contribution from thermal bremsstrahlung. Measurements of high circular polarization confirm its classification as a Polar with a magnetic field strength of 56 MG. The average visual magnitude of RX J1313.2–3259 is $V \simeq 16^{\rm m}$, for its distance we get $\simeq$ 200 pc.

**Key words:** stars: cataclysmic variables – stars: magnetic fields – stars: individual: RX J1313.2–3259 – binaries: close – X-rays: stars – accretion

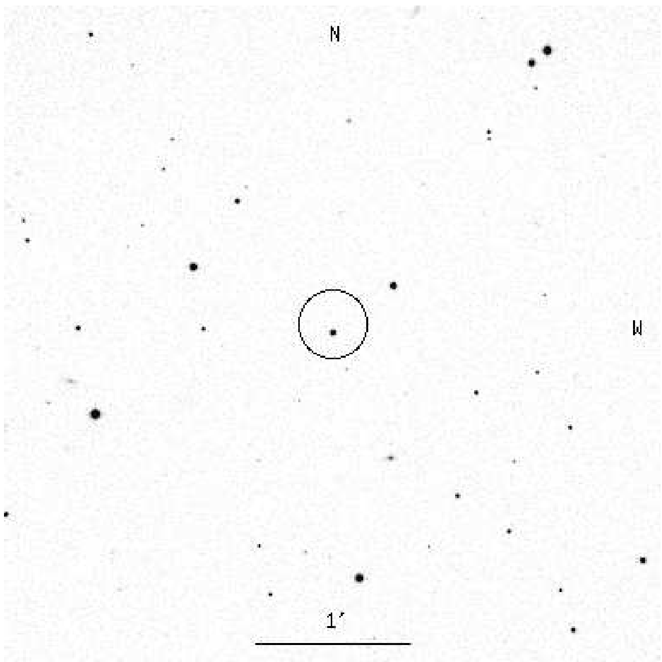


**Fig. 1.** V-band CCD image of RX J1313.2–3259. The X-ray error circle from the RASS refers to the 90% confidence level. The position of the optical counterpart is $\alpha_{2000} = 13^{\rm h}13^{\rm m}17\overset{\rm s}{.}1$, $\delta_{2000} = -32°59'12''$, the average visual magnitude $V \simeq 16^m$.

## 1. Introduction

Polars or AM Herculis binaries belong to the class of cataclysmic variables. They consist of a low mass main sequence star filling its critical Roche lobe and a magnetic white dwarf accreting matter from its companion. The strong magnetic field channels the accretion flow into a small area on the surface of the white dwarf. In this area the temperature rises to values of several 100 000 K and shifts the emission of reprocessed radiation into the soft X-ray regime. Therefore an efficient way to detect these systems is to search the sky for (highly) variable extreme ultraviolet or soft X-ray emitters. The great success of ROSAT, ASCA, and EUVE in detecting these systems is demonstrated by the fact, that before ROSAT only 17 Polars were known (Cropper 1990) whilst as of today this number has increased to 63. Other sources of radiation in these systems are thermal bremsstrahlung emission from the accretion column, observed at higher X-ray energies (typically 10 to 20 keV), cyclotron emission from the accretion column due to the strong magnetic field, often dominating the optical regime, and radiation from the secondary star, strongest in the infrared and sometimes only

*Send offprint requests to*: hcthomas@mpa-garching.mpg.de
⋆ Based in part on observations collected at the European Southern Observatory, La Silla, Chile with the ESO/MPI 2.2m telescope in MPI time and with various telescopes in ESO time (ESO Nos. 50.6-017, 50.6-021, 54.D-0698, 55.D-0383, 56.D-0552, 56.D-0561, 61.D-0415).

**Table 1.** List of observations. Columns denote: (1) and (2) the time of the observation, (3) and (4) the telescope and instrument used, (5) the type of observation (spec.: spectrophotometry, point.: X-ray pointing, phot.: photometry, sp.pol.: spectropolarimetry), (6) the spectral range or the filters used, (7) the FWHM resolution (spectroscopy only), (8) the number of spectra or V filter data obtained, (9) the time span for the observation, and (10) the exposure time for the individual measurements.

| (1) date | (2) JD | (3) telescope | (4) instrument | (5) activity | (6) spectral range | (7) res. | (8) no. | (9) dur. | (10) exp. |
|---|---|---|---|---|---|---|---|---|---|
| Jan 1991 | 2 448 270 | ROSAT XRT | PSPC | RASS | 0.1-2.4 keV | | 1 | 1.5 days | 8 min |
| Aug 1991 | 2 448 500 | ESO/MPI 2.2m | EFOSC 2 | spec. | 3500-9000 Å | 40 Å | 1 | 10 min | 10 min |
| Jan 1992 | 2 448 632 | ESO/MPI 2.2m | EFOSC 2 | spec. | 3500-9000 Å | 40 Å | 9 | 4.1 days | 5 min |
| Jan 1992 | 2 448 633 | ESO/MPI 2.2m | EFOSC 2 | spec. | 3500-5400 Å | 10 Å | 23 | 1.1 days | 10 min |
| Jul 1992 | 2 448 832 | ROSAT XRT | PSPC | point. | 0.1-2.4 keV | | 0 | 2.4 days | 3.8 hours |
| Aug 1992 | 2 448 859 | ESO/MPI 2.2m | EFOSC 2 | spec. | 3500-5400 Å | 9 Å | 22 | 6.0 days | 10 min |
| Aug 1992 | 2 448 859 | ESO/MPI 2.2m | EFOSC 2 | spec. | 5800-8400 Å | 12 Å | 21 | 6.0 days | 5 min |
| Feb 1993 | 2 449 035 | ESO 1.0m | Photom. | phot. | UBVRI | | 12 | 2.0 days | 2 min |
| Feb 1993 | 2 449 037 | ESO/MPI 2.2m | EFOSC 2 | spec. | 3500-9000 Å | 25 Å | 1 | 5 min | 5 min |
| Feb 1993 | 2 449 038 | ESO/MPI 2.2m | EFOSC 2 | phot. | V | | 10 | 2.0 days | 30 sec |
| Feb 1993 | 2 449 038 | ESO/MPI 2.2m | EFOSC 2 | spec. | 5800-8400 Å | 8 Å | 27 | 2.1 days | 10 min |
| Aug 1993 | 2 449 224 | ESO/MPI 2.2m | EFOSC 2 | spec. | 3500-9000 Å | 25 Å | 1 | 15 min | 15 min |
| Jul 1994 | 2 449 566 | ROSAT XRT | HRI | point. | 0.1-2.4 keV | | 0 | 3.3 days | 4.9 hours |
| Feb 1995 | 2 449 752 | ESO 1.0m | Photom. | phot. | BVR | | 102 | 4.2 hours | 2 min |
| Jul 1995 | 2 449 902 | ESO/MPI 2.2m | EFOSC 2 | spec. | 3500-5400 Å | 8 Å | 22 | 1.1 days | 10 min |
| Jul 1995 | 2 449 902 | ESO/MPI 2.2m | EFOSC 2 | spec. | 3800-9100 Å | 35 Å | 6 | 2.0 days | 5 min |
| Jul 1995 | 2 449 907 | ESO 1.54m | Dir. Im. | phot. | BVR | | 213 | 1.1 days | 1 min |
| Dec 1995 | 2 450 075 | ESO/MPI 2.2m | EFOSC 2 | spec. | 3800-9100 Å | 30 Å | 14 | 2.0 days | 10 min |
| Jan 1996 | 2 450 097 | ESO/Dutch 0.9m | Dir. Im. | phot. | VRI | | 242 | 4.2 days | 30 sec |
| Mar 1997 | 2 450 511 | ESO/MPI 2.2m | EFOSC 2 | spec. | 3600-10200 Å | 50 Å | 39 | 2.2 days | 10 min |
| Mar 1997 | 2 450 511 | ESO/MPI 2.2m | EFOSC 2 | spec. | 6440-8360 Å | 5 Å | 15 | 4.2 hours | 15 min |
| Mar 1997 | 2 450 513 | ESO/MPI 2.2m | EFOSC 2 | spec. | 3600-5200 Å | 6 Å | 16 | 4.6 hours | 15 min |
| May 1998 | 2 450 935 | ESO 3.6m | EFOSC 2 | phot. | BVR | | 37 | 4.6 hours | 1 min |
| May 1998 | 2 450 937 | ESO 3.6m | EFOSC 2 | sp.pol. | 3600-7490 Å | 5 Å | 9 | 2.7 hours | 15 min |

being detectable, if the system is in a state of low accretion. Detailed discussions of these systems can be found in the books by Warner (1995) and Campbell (1997). Early reviews on the basis of the new ROSAT data have been presented among others by Beuermann & Thomas (1993), Watson (1994), Beuermann & Burwitz (1995), and Schwope (1995), a more recent one by Beuermann (1997). The distribution of Polars in the solar neighborhood was investigated by Thomas & Beuermann (1997). An identification program based on a complete sample of the brightest soft X-ray sources from the RASS (Voges et al. 1999) at high galactic latitudes (Thomas et al. 1998) led to the detection of RX J1313.2–3259.

## 2. Observations

Starting 12 January 1991 the position of RX J1313.2–3259 in the sky was scanned by the ROSAT XRT with the PSPC as detector. During 20 satellite orbits with a total exposure time of 485 s the object was detected with a mean count rate of 1.8 cts $s^{-1}$ and a hardness ratio $HR1 = -0.85$[1]. On a finding chart produced from the COSMOS scans of the SERC-J plates at ROE (Yentis et al. 1992) a V $= 16^{\rm m}$ star was found to be the likely optical counterpart, at a distance of $\simeq 3''$ from the X-ray position (Fig. 1). A low resolution spectrum taken on 31 August 1991 at the ESO/MPI 2.2m telescope showed strong Balmer and helium line emission thus confirming this identification. A list of all observations collected until now can be found in Table 1.

### 2.1. X-ray photometry and spectroscopy

From the RASS data a photon event table was extracted which covered $50 \times 50$ arcmin$^2$ around the X-ray position of the source. Using the EXSAS software package provided by the MPE Garching (Zimmermann et al. 1994) for the extraction of source photons in a circle of $250''$ radius centered on the source and background photons in a circle of $400''$ radius in scan direction we obtained the light curve shown in Fig. 2 and the mean spectrum inserted in Fig. 4.

[1] $HR1 = (H - S)/(H + S)$ with $H$ and $S$ the count rates in the hard and soft energy intervals $0.5 - 2.4$ keV and $0.1 - 0.4$ keV, respectively.

Phasing of the light curve has been obtained from Eq. (2) based on optical observations (see Sect. 3.2), so phase zero corresponds to the inferior conjunction of the secondary star. The error in the period results in a phase error below 0.01, therefore the cycle count is correct. The data are sampled from nine different orbital cycles of the binary. The mean count rate obtained from the light curve is 1.94 cts $s^{-1}$. In one ROSAT orbit a count rate far above the average (6.5 cts $s^{-1}$) was measured. We consider this as a singular event not typical for the orbital variation. Without this point the mean count rate drops to 1.68 cts $s^{-1}$. In order to show that the light curve is not dominated by changes between binary orbits we have used two different symbols in Fig. 2 for the first and second half of the observation. A period search without the point at 6.5 cts $s^{-1}$ revealed a likely period of $254 \pm 7$ min. It should be noted that at no phase did the count rate drop to zero, so the accretion area giving rise to the X-ray emission never completely vanishes from view behind the horizon of the white dwarf. The alternative of a second accretion area contributing to the X-ray flux seems to be ruled out by the results of our spectropolarimetry, which shows no change of sign in the circular flux (see Sect. 2.3).

In two subsequent pointings with the ROSAT PSPC (July 1992) and HRI (July 1994) as detectors the source was observed with count rates of 0.036 PSPC cts $s^{-1}$ (hardness ratio $HR1 = 0.28$) and 0.010 HRI cts $s^{-1}$ (corresponding to $\simeq 0.06$ PSPC cts $s^{-1}$). This is a reduction in the count rate by factors 50 (1992) and 30 (1994) compared to the RASS. Phase binning of these data resulted in the lightcurves shown in Fig. 2. Again we note that the site of the X-ray emission always remains in view of the observer.

Fitting the RASS spectrum with a blackbody and a thermal bremsstrahlung component together with possible interstellar absorption resulted in a blackbody temperature of 58 eV and a column density of $9 \cdot 10^{19}$ H-atoms $cm^{-2}$. The uncertainties for these parameters are depicted in Fig. 3. The (unabsorbed) contributions of the two components to the total flux in the ROSAT window (0.1 to 2.4 keV) amount to $1.14 \cdot 10^{-11}$ erg $cm^{-2}s^{-1}$ and $0.07 \cdot 10^{-11}$ erg $cm^{-2}s^{-1}$, respectively. For the temperature of the thermal bremsstrahlung component we assumed a value of 10 keV, since this cannot be derived from the spectral data. The resulting unabsorbed spectra are shown in Fig. 4 as dotted lines. Separating the count rate into the two components one obtains 1.70 cts $s^{-1}$ for the blackbody component and 0.07 cts $s^{-1}$ for the thermal bremsstrahlung component. The flux ratio $F_{\rm brems}/F_{\rm bb}$ in the ROSAT band is 0.06, integrated over all frequencies it increases to 0.16. The uncertainty in these values is about a factor 2.

The spectral fit to the data from the PSPC pointing gave a blackbody temperature of 50 eV, an unabsorbed flux of $4.7 \cdot 10^{-14}$ erg $cm^{-2}s^{-1}$ for the blackbody component and $9.1 \cdot 10^{-13}$ erg $cm^{-2}s^{-1}$ for the thermal bremsstrahlung component, with large uncertainties and a high correlation between flux and temperature of the blackbody fit (see Sect. 3.4). Here we again fixed the temperature for the thermal bremsstrahlung component to 10 keV, and the column density to the value obtained during the RASS. The data are also shown in Fig. 4.

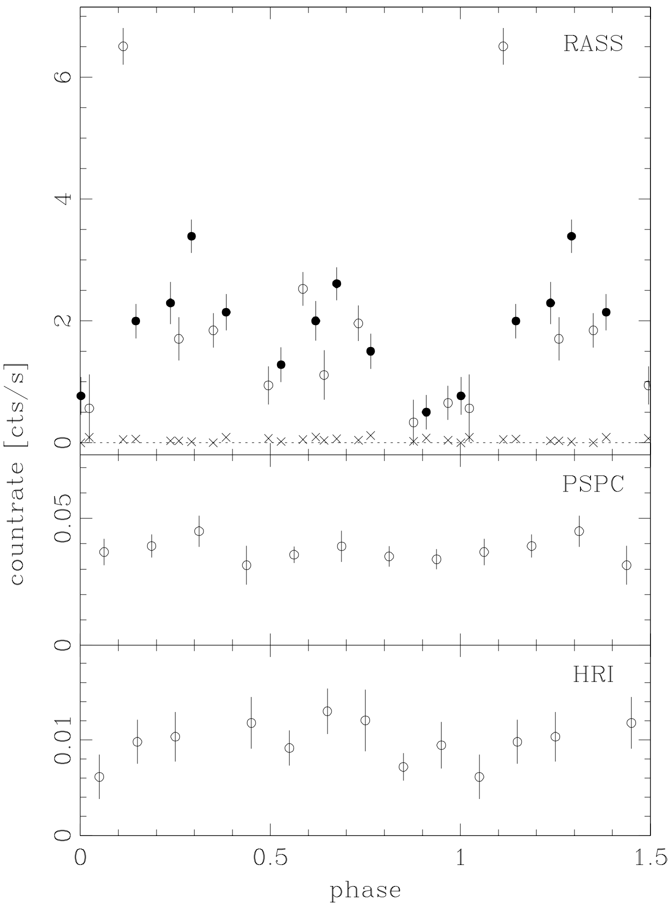


**Fig. 2.** X-ray light curve of RX J1313.2–3259. The upper panel shows the source during the RASS (first half of observation: filled circles, second half: open circles) together with the measured background (crosses), the lower panels during two subsequent pointings with the PSPC and the HRI as detectors, respectively. For the preliminary period determination the single high datum at 6.5 cts $s^{-1}$ has been ignored. The phases are computed from Eq. (2) in Sect. 3.2.

### *2.2. Optical photometry*

Sequences of direct images in different filters were taken at several epochs (see Table 1). To demonstrate the long-term variability of RX J1313.2–3259 we have plotted in Fig. 5 the mean values of $V$ in the different runs together with the range of variability defined by the magnitudes which bracket 90% of the measurements in the corresponding observing run. Added to this plot are V-magnitudes from spectroscopy, obtained by folding the mean spectrum of each observing run with the sensitivity of the V-filter

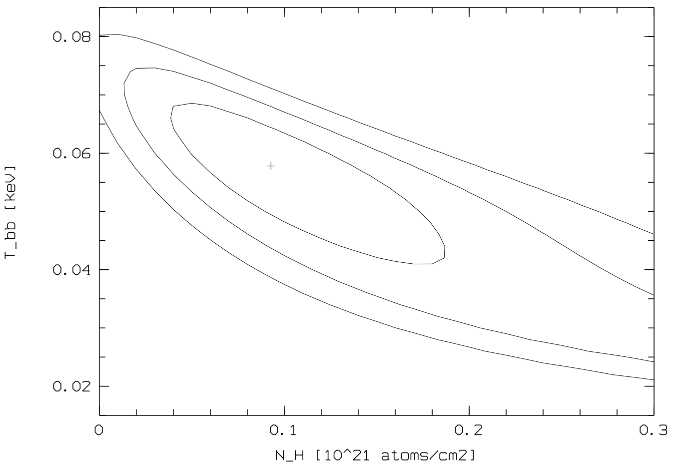


**Fig. 3.** Confidence levels for the X-ray spectral fit of RX J1313.2–3259. The 1, 2, and $3\sigma$ ranges for the fit parameters blackbody temperature and column density are shown together with the fit result (cross).

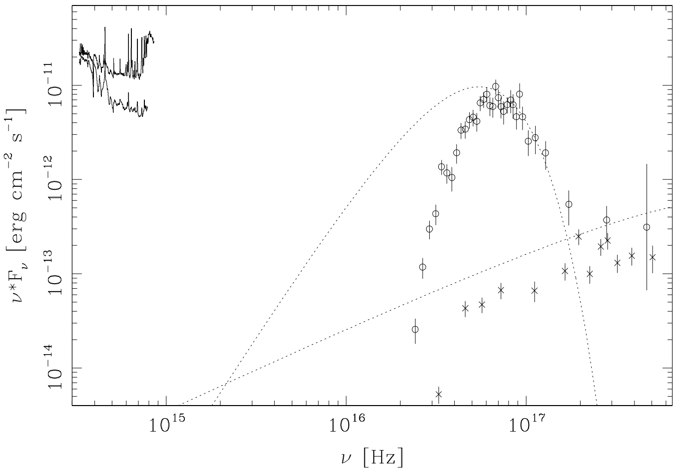


**Fig. 4.** Overall observed spectrum of RX J1313.2–3259. The optical spectra shown at low frequencies were obtained in Feb. 93 (high state) and in Dec. 95 (low state). In the X-ray regime the RASS data are shown as circles, the PSPC pointing data as crosses. The dotted lines give the unabsorbed blackbody and bremsstrahlung components of the X-ray spectral fit to the RASS data.

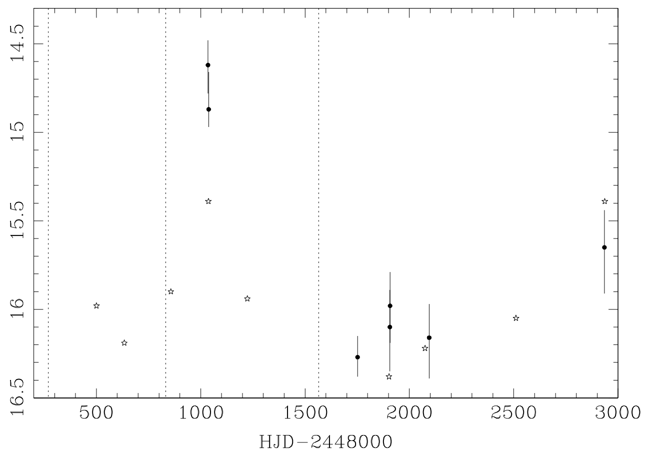


**Fig. 5.** Long-term light curve of RX J1313.2–3259. Photometric observations are marked with filled dots (mean values) and a vertical bar (90% range), magnitudes derived from mean spectra (less accurate) by stars. The dotted lines show the times of X-ray observations (RASS, PSPC, HRI).

(a flux of $3.64 \cdot 10^{-9}\,\mathrm{erg\,cm^{-2}s^{-1}\AA^{-1}}$ corresponds to zero magnitude, see Bessell 1979). The dotted lines indicate the times of the X-ray observations (RASS, PSPC pointing, and HRI pointing). Typically RX J1313.2–3259 is found at $V \simeq 16^{\mathrm{m}}$ and brightened only for short episodes near HJD 2 449 036 (Feb. 93) and HJD 2 450 936 (May 98).

The orbital variation of RX J1313.2–3259 in the V-band is displayed in Fig. 6. Different symbols identify the different observing runs which are listed at the bottom of the figure. The lightcurves are clearly of different character in the bright (Feb. 93, May 98) and faint (all other) states of RX J1313.2–3259. While the bright states show only one minimum per orbit, the variation in the faintest state (Feb. 95) almost follows a sinusoidal variation with two minima per orbit. With increasing brightness the flux first increases outside the primary minimum (near phase zero) and starts to deviate from its value around the primary minimum for the bright states only.

It is worth mentioning that the observations in Feb. 93 were collected in six subsequent nights with two different instruments and that during this high state episode the orbital-averaged flux decreased by 0.07 mag per day, suggesting a characteristic duration of the high state of a few weeks. The orbital light curve for the Feb. 93 data in Fig. 6 (diamonds) was obtained by subtracting a linear trend from the data. The fitted light curve (dotted line) represents a sinusoidal fit to the detrended data.

### *2.3. Optical spectroscopy and spectropolarimetry*

Time sequences of spectra at different resolutions were obtained at 9 epochs as listed in Table 1 and displayed in Fig. 5 (stars). We first display in Fig. 7 the low resolution spectra from Feb. 93 (brightest state) and from July 95 (faintest state). Both spectra clearly show the contribution of a late-type star to the flux at the red wavelengths, identifiable through its TiO absorption troughs. The emission lines of hydrogen and helium are visible in both spectra, with He II $\lambda$4686 strongly reduced in the fainter spectrum.

Complete coverage of the orbit in one night could be achieved for the observation run in March 97 (intermediate state) only. Medium resolution spectra in the blue (3600–5200 Å) and in the red (6440–8360 Å) were analyzed for Doppler shifts in their emission and absorption lines. The most accurate results were obtained for

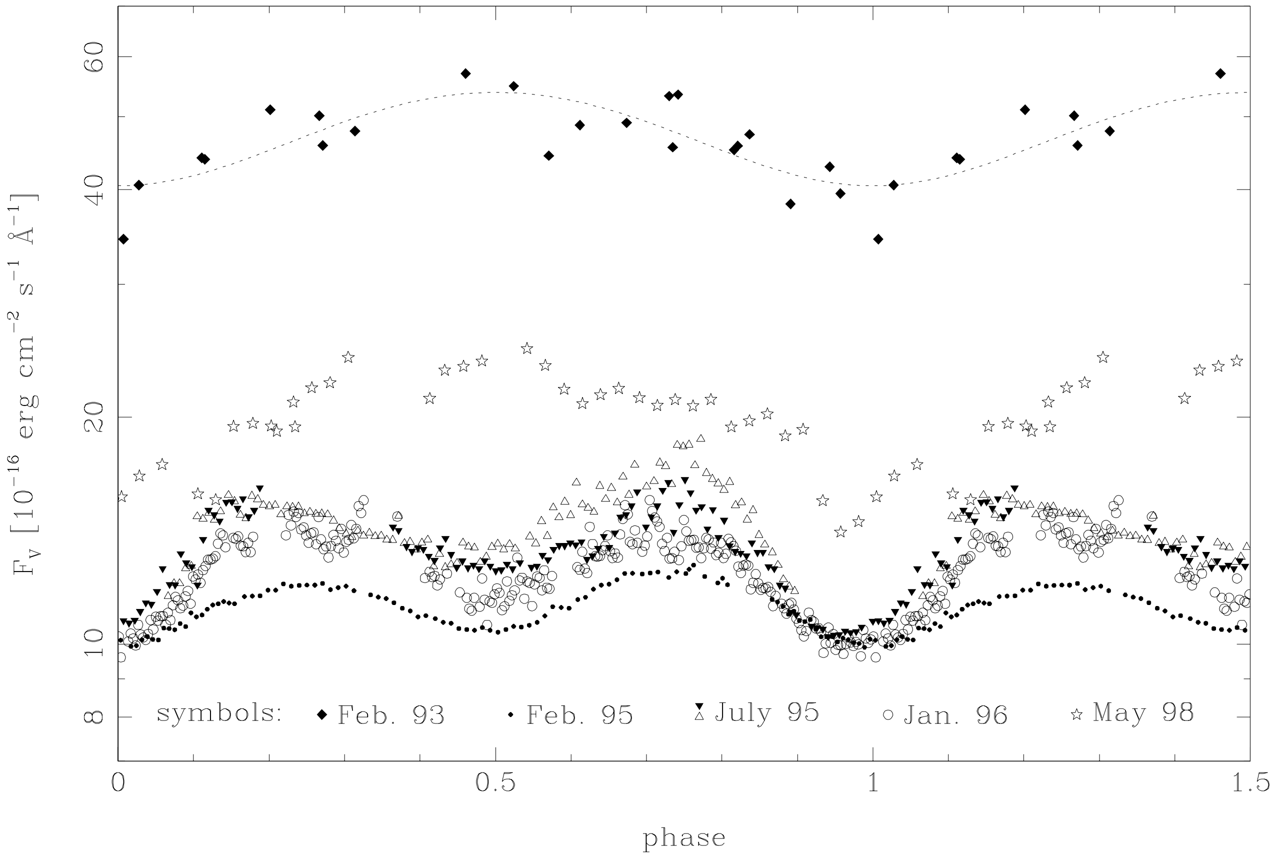


**Fig. 6.** Phase-folded lightcurves at different observing times as given at the bottom of the plot. For the dotted line see text in Sect. 2.2. The phases are computed from Eq. (2) in Sect. 3.2.

**Table 2.** Results from double Gaussian fits. The columns list the fitted emission line, the velocity amplitudes in km/s and phases for blue-to-red zero crossing both for the narrow and the broad component and the line flux ratio of minimum to maximum for the narrow component.

| line | $v_{\rm narrow}$ | $\phi_0$ | $v_{\rm broad}$ | $\phi_0$ | flux ratio |
|---|---|---|---|---|---|
| H$\alpha$ | 100 | 1.011 | 397 | 0.717 | 0.41 |
| H$\beta$ | 109 | 0.994 | 353 | 0.709 | 0.31 |
| H$\gamma$ | 97 | 0.976 | 485 | 0.687 | 0.29 |
| H$\delta$ | 106 | 0.992 | 434 | 0.704 | 0.27 |
| He I $\lambda$4026 | 101 | 0.933 | 624 | 0.673 | 0.22 |
| He I $\lambda$6678 | 92 | 0.957 | 498 | 0.714 | 0.24 |
| He II $\lambda$4686 | 63 | 0.937 | 512 | 0.712 | 0.26 |
| Ca II K | 117 | 0.972 | 567 | 0.714 | 0.24 |

the red spectra. Fitting the H$\alpha$ emission line with a double Gaussian profile splits the line into a narrow (average FWHM 5.9 Å, unresolved) and a broader (average FWHM 17 Å) component. The resulting radial velocities are plotted in Fig. 8, upper panel. The average radial velocities of three absorption lines (Na I $\lambda$8183, 8195 and K I $\lambda$7699) are shown in the same panel. In the lower panels of Fig. 8, the fluxes in the narrow emission component of He I $\lambda$6678 and the absorption line of K I $\lambda$7699 are displayed together with results from irradiation computations (see Sect. 3.2). The measured fluxes of the absorption line are very sensitive to the assumed level of the continuum near this line and may be in error by up to 30%. We also measured the fluxes in the narrow emission components of H$\alpha$, H$\beta$, H$\gamma$, H$\delta$, He II $\lambda$4686, He I $\lambda$4026, and Ca II K by fitting double Gaussians to the profiles. In Table 2 the velocity amplitudes and phases for the blue-to-red zero crossings are given for the two components together with the line flux ratios (minimum to maximum) of the narrow components. The phases were derived from the ephemeris given in Sect. 3.2. The minimum emission line flux stays finite for all of these lines. In this respect, all lines behave similarly to He I $\lambda$6678 in Fig. 8.

During the observation in Dec. 95 the source was in a low state, which allows for a separation of the spectral flux into the different contributions from the M-star, the accretion area, and the white dwarf. The results of this analysis will be discussed in Sect. 3.3. The spectra taken during another low state in Jan. 92 are not suited for this kind of analysis because they cover less than half an orbit and their flux calibrations are unreliable.

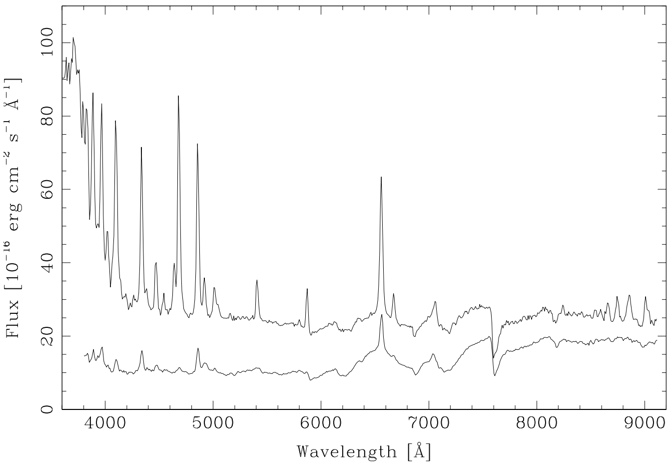


**Fig. 7.** Spectra at low resolution from two different observing runs. The brighter spectrum was taken in Feb. 93, the other is the mean of six spectra obtained in July 95.

For the observation in May 98 (high state) EFOSC 2 was equipped with the Wollaston prism and a quarterwave plate, using Grism B300. The sequence of $2 \times 9$ spectra covers only 60% of the orbital period. Circularly polarized fluxes have been obtained by taking the difference between the two spectra produced by the Wollaston prism (Fig. 9). All spectra show circular polarization of negative sign only. We find, that two maxima of the polarized flux, at $\simeq 5000$ Å and $\simeq 6600$ Å, are present in all spectra except near phase 0 where the viewing angle is smallest with respect to the axis of the accretion funnel. In addition, a third maximum of the polarized flux occurs at $\simeq 3950$ Å over the restricted phase interval of 0.3 to 0.5. We will argue below that these are the 3$^{\rm rd}$, 4$^{\rm th}$, and 5$^{\rm th}$ harmonic in a field of about 56 MG and that the different phase behavior arises from optical depth and geometric effects (Sect. 3.3).

Spectra taken during the other observing runs have been analyzed for radial velocities, flux contribution from the secondary star, and cyclotron emission. Because of lower resolution, incomplete orbital coverage, or less favorable observing conditions they mainly helped to reinforce and confirm the results obtained from the March 97 data and are important for excluding possible alias periods.

## 3. Results

### *3.1. A distance estimate*

In all low resolution spectra the TiO absorption bands from the secondary are easily recognized. We therefore use the calibration method decsribed in Beuermann & Weichhold (1999) to determine the surface flux from the flux difference between 7165 and 7500 Å. In July and Dec. 95 RX J1313.2–3259 was in a low state, so we used the flux

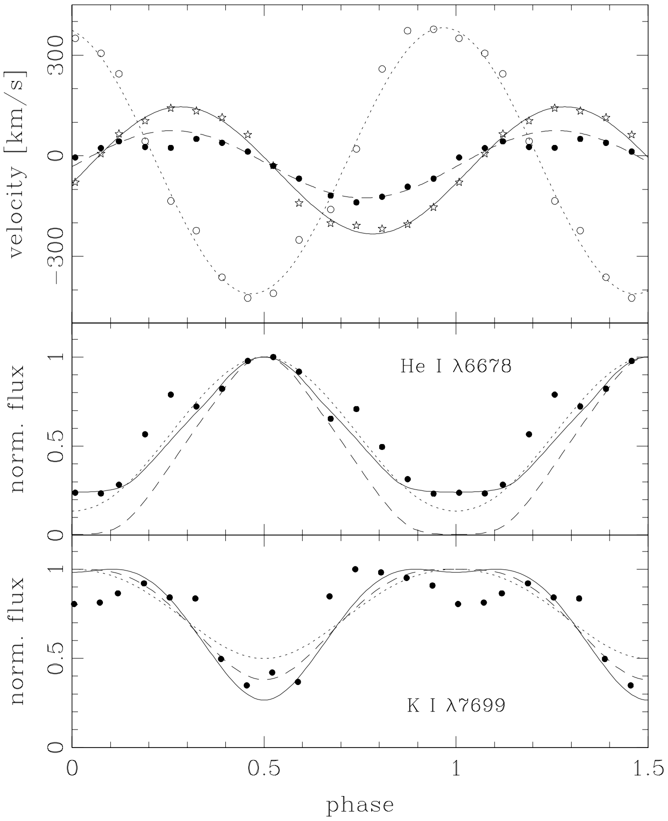


**Fig. 8.** Line properties extracted from spectra taken in Mar. 97. *Upper panel:* radial velocities averaged from measurements of three absorption lines (stars), from the narrow component of the Hα emission line (filled circles), and the broad component of the Hα emission line (open circles). The solid, dashed, and dotted lines give the sinusoidal fits to the data. *Middle panel:* normalized line flux of the He I λ6678 narrow emission component together with results from irradiation computations for three different inclinations (solid: 66°, dashed: 52°, dotted: 31°, see Sect. 3.2). *Lower panel:* normalized line flux of the K I λ7699 absorption line together with results from irradiation computations for the same inclinations.

differences as observed. For the Mar. 97 data we first estimated the gradient of the cyclotron emission between 7165 Å and 7500 Å by subtracting suitably scaled spectra of the M-dwarf Gl 207.1 and corrected the measured flux differences for that. We also tried to fit spectra of other M-dwarfs (e.g. Gl 205, Gl 352) but with less satisfactory results. From these 35 spectra we obtained a mean value of $9.7 \pm 1.1 \cdot 10^{-16}$ erg cm$^{-2}$s$^{-1}$Å$^{-1}$ for the flux difference. This value is reduced by 2% if we exclude all spectra with phases between 0.25 and 0.75, i.e. looking at the unilluminated backside of the secondary. In the following we use a value of $9.5 \cdot 10^{-16}$ erg cm$^{-2}$s$^{-1}$Å$^{-1}$.

Filling its critical Roche lobe the secondary must have a mean density of $\rho/\rho_\odot = 4.46$ for a system period of 4.19 h. This value depends slightly on the mass ratio but the distance changes by no more than 2% for white dwarf

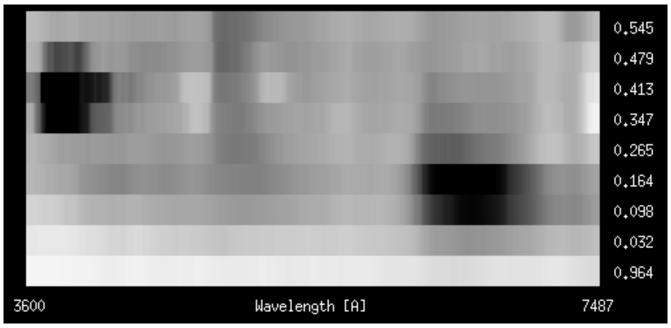


**Fig. 9.** Circularly polarized flux extracted from spectra taken in May 98. The grayscale plot displays fluxes between 0 (white) and $-6{\cdot}10^{-16}$ erg cm$^{-2}$s$^{-1}$Å$^{-1}$ (black), orbital phases are given on the right-hand side. The image is smoothed in order to remove the contributions from the emission lines.

masses between 0.5 and 1.2 $M_\odot$. Assuming the secondary to be a main-sequence star the stellar models of Baraffe et al. (1998) suggest a mass of 0.51 $M_\odot$ and a radius of 0.486 $R_\odot$, with a slight dependence on mass ratio. However, the secondary, due to its mass-loss history, may be out of thermal equilibrium and therefore have a lower mean density than a main-sequence star of the same mass. Comparing the low-state spectra to those of several M-stars we estimate the spectral type to be M2.5 ±0.5. Since the spectral type does not change drastically for stars out of thermal equilibrium (Kolb & Baraffe 1999), we obtain an estimate for the mass of the secondary from a comparison with models of Baraffe et al. (1998): $M_2/\mathrm{M}_\odot \simeq 0.45$. Using the relation between spectral type and the surface brightness $F_{\mathrm{TiO}}$ by Beuermann & Weichhold (1999) we arrive at a distance of

$$200 \pm 17\ \mathrm{pc} \cdot (M_2/0.45\,\mathrm{M}_\odot)^{1/3}. \tag{1}$$

### *3.2. System parameters*

The orbital period of RX J1313.2–3259 was obtained from a sinusoidal fit to the radial velocity measurements of the absorption lines Na I λ8183,8195 and K I λ7699, obtained in Aug. 92, Feb. 93, and Mar. 97. Possible aliases have been checked against other radial velocity measurements obtained at many different epochs (see Table 1). The zero point for the resulting ephemeris is defined as the blue-to-red zero-crossing of the radial velocity curves. The fits to the narrow emission line components of the Mar. 97 data give a slightly earlier zero point than the absorption line data (difference in phase: $0.06 \pm 0.03$) and we have used the mean of both data sets. The resulting ephemeris is (errors of the last digits are given in brackets):

$$T = \mathrm{HJD}\ 2\,448\,632.4435(43) + 0.174\,592\,09(15)\ E \tag{2}$$

The relatively large error in the zero point reflects the difference in determining the blue-to-red zero-crossing from both the narrow emission and the absorption line measurements. The total time span between our first and last observation amounts to 2667 days or 15276 cycles. Thus the maximum error in the phasing calculated from the error for the period is 0.013, which excludes any errors in the cycle count.

The measurements shown in the two lower panels of Fig. 8 clearly demonstrate that the narrow emission line flux is stronger and the absorption line flux weaker than average when the illuminated side of the secondary is in view of the observer. Such a behavior can be understood with the irradiation model of Beuermann & Thomas (1990). Using the amplitude of $185 \pm 9$ km/s measured for the absorption lines the model determines the inclination angle as a function of mass ratio. We have assumed that the contribution to the absorption line flux from the illuminated side is negligible. For primary masses of 0.5 and 1.1 $M_\odot$ we obtain inclinations of 52° and 31°, respectively, taking 0.45 $M_\odot$ for the mass of the secondary. The corresponding velocities for the emission lines are then 51 and 98 km/s. Looking at the measured values (Table 2) this would favor the low inclination and so a high primary mass. A low inclination also roughly fits the observed line fluxes, an example is shown in Fig. 8 (middle panel, dotted line). For the inclination of 66° derived below (Sect. 3.3) this is not the case. But if we assume that a substantial contribution to the line flux comes from the unilluminated side of the secondary the situation changes. To reproduce the observed average amplitude of 102.6 km/s for the narrow emission lines, $\simeq 55\%$ of the line flux (averaged over the surface of the secondary) must be generated by illumination. We then obtain the line flux variation displayed in Fig. 8 (middle panel, solid line), which fits the observed variation best, except for those measurements where the radial velocity curves of broad and narrow component cross each other and therefore a separation into the two components is difficult to achieve. While this result depends only weakly on the assumed inclination it shows that the observed line flux and velocity amplitude for the narrow emission are consistent with a high inclination if part of the emission line flux is generated on the unilluminated side of the secondary.

### *3.3. Cyclotron emission*

For the data taken during a low state in Dec. 95, we represent the spectral flux in the 14 individual low-resolution spectra by the sum of a Rayleigh-Jeans spectrum, an M-star spectrum, and a cyclotron spectrum. This was done by adjusting the Rayleigh-Jeans to the flux between 4040 and 4080 Å and the M-star template to the flux difference between 7165 and 7500 Å. (As discussed in Sect. 3.1 the best M-star template is that of the M3 star Gl 207.1). Subtracting these two contributions we are left with the cyclotron spectra shown in Fig. 10. The variation of the

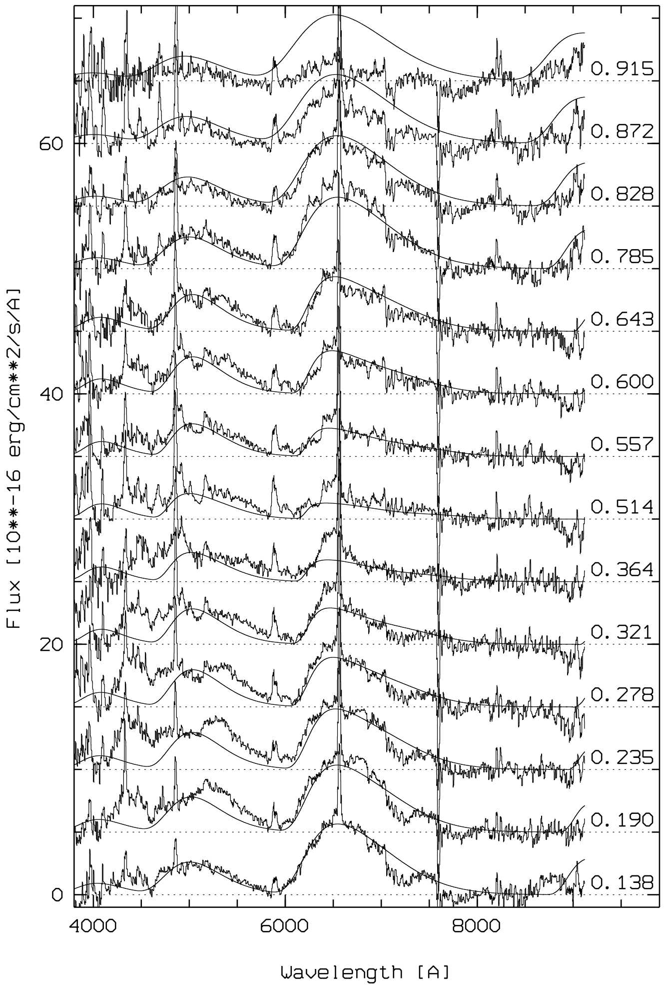


**Fig. 10.** Cyclotron flux extracted from spectra taken in Dec 95. The model fits are discussed in Sect. 3.3, orbital phases are given on the right-hand side.

Rayleigh-Jeans component in the V-band is roughly sinusoidal and can be fitted with a mean of $3.1\pm0.1$ and an amplitude of $0.3\pm0.1$, both in units of $10^{-16}\,\mathrm{erg\,cm^{-2}s^{-1}\AA^{-1}}$, the maximum occuring at phase $0.01 \pm 0.4$. Such a variation indicates heating of an area around the accretion spot (see Sect. 3.3). The flux of the M-star displays maxima at phases near quadrature. The origin of the these variations must be due to ellipsoidal modulation from the M-star. The flux ratio between phases 0.5 (primary minimum) and 0.25/0.75 (maxima) amounts to $0.85 \pm 0.02$.

To model the Dec. 95 variation of cyclotron flux with orbital phase we adapted the emission of an isothermal homogeneous plasma slab (Barrett & Chanmugam 1985) to the data. The input parameters were the magnetic field strength $B$, the plasma temperature $T$, the inclination $i$ of the system, the angle $\beta_f$ between the rotation axis and the field direction, the angles $\beta_s$ and $\psi_s$ describing the location of the accretion region (relative to the rotation axis and the line connecting the two stars), and the dimensionless thickness $\Lambda$ and the area $A_{\mathrm{s}}$ of the accretion region. From the phasing of the broad emission lines we took the azimuthal angle between field direction and direction to the companion $\psi_f$ to be 17°. The fit shown in Fig. 10 required $B = 56\,\mathrm{MG}$, $T = 10\,\mathrm{keV}$, $i = 66°$, $\beta_f = 7°$, $\beta_s = 24°$, $\psi_s = 18°$, $\Lambda = 26$, and $A_{\mathrm{s}} = 8.2 \cdot 10^{16}\ \mathrm{cm}^2$ (for a distance of 200 pc). It was obtained in a iterative procedure starting with a coarse grid of cyclotron spectra which allowed to fix $B$, $T$, $i$, and $\beta_f$ and then refining the grid for the other parameters. The poor fit at phase 0.915 may be the result of absorption by the accretion stream which is in front of the accretion area around phase 0.95. The rather high inclination can only be made consistent with the results from the irradiation model for a white dwarf mass of $0.39\,\mathrm{M}_\odot$ (see Sect. 3.5). The values of $\beta_f$ and $\beta_s$ are in conflict with the assumption of a pure dipolar field configuration because that requires $\beta_f > \beta_s$. Also this simple model does not reproduce the spectral shape at short wavelengths, probably due to a more complicated accretion geometry than used here.

Using the parameters derived above we computed the gravity darkening in the Roche geometry. For the ratio of primary minimum to maximum we obtained a value between 0.87 (without limb-darkening) and 0.83 (50% limb-darkening), in agreement with the value for the ellipsoidal variation deduced above.

For the values of $i$, $\beta_s$, and $\psi_s$ the sinusoidal variation of the Rayleigh-Jeans component can be explained assuming a constant contribution from the white dwarf photosphere plus a varying contribution from the accretion area. The fluxes in the V-band then amount to 2.8 and 0.85, respectively, both in units of $10^{-16}\,\mathrm{erg\,cm^{-2}s^{-1}\AA^{-1}}$. At the derived distance the constant flux gives an absolute magnitude of $\mathrm{M_V} = 11.3^{\mathrm{m}}$, corresponding to a photospheric temperature of $\simeq 14\,000\,\mathrm{K}$. The flux ratio of the variable to constant component in an accretion area occupying a fraction $f$ on the white dwarfs surface requires a temperature which is a factor $0.74\ f^{-0.25}$ higher than the temperature of the white dwarf, in reasonable aggreement with the results of Gänsicke et al. (1999).

We also tried to fit the spectropolarimetric data from May 98, which do not suffer from the uncertainties introduced by the subtraction of other flux contributions. But because of the incomplete orbital coverage we can only state that magnetic field strength, inclination, and field direction are similar, while the thickness $\Lambda$ must be somewhat larger to produce the high circularly polarized flux at 3950 Å around phase 0.4 (see Fig. 9). We plan to repeat these observations, which will then allow us to check the system parameters derived above. Cyclotron spectra extracted from the Mar. 97 data show similar variations with phase as the data of Dec. 95, but the removal of other flux contributions introduced too large an uncertainty, so we did not try to fit cyclotron spectra to that dataset.

These considerations also allow us to qualitatively understand the behavior of the V-flux variations (Fig. 6). In a low state both the cyclotron flux and the ellipsoidal variations of the secondary cause a light curve with two maxima during one orbit, while in a high state the contribution of the secondary is negligible and the cyclotron flux contribution most likely comes from a more extended accretion area. The minimum around phase 0.5 which resulted from a viewing angle close to 90° will then be filled in because of contributions from other parts of the accretion area at lower viewing angles.

### *3.4. X-ray emission*

We now turn to the X-ray light curves and spectra obtained during the RASS and the two ROSAT PSPC and HRI pointed observations. Since the inclination is larger than the field line direction it is expected that at least part of the X-ray flux is absorbed by the stream of matter towards the white dwarf. This explains the low flux around phase 0.95 both in the RASS and to some degree in the HRI pointing. The reduction in the count rate by a factor 50 between the RASS and the PSPC pointing and the corresponding change in the hardness ratio $HR1$ from −0.96 to 0.28 could partially be the result of a lower blackbody temperature. Although the best fit temperature for the pointing is 50 eV ($\chi^2$/d.o.f. 22/10), with a reduction of the blackbody flux by a factor 230 compared to the RASS, the fit allows for much higher blackbody fluxes if the temperature would be lower: at 15 eV, the total blackbody flux decreases by a factor 14 only compared to the RASS ($\chi^2$/d.o.f. 27/11). This is of the same order as the reduction in cyclotron flux between the observations in Feb. 93 and Dec. 95 (factor 7.4). The contribution of the bremsstrahlung flux to the PSPC pointed data is reduced by a factor 2.3 compared to the RASS.

### *3.5. Masses of the components*

The masses determined above are in conflict with present understanding of stable mass transfer. For donor stars with masses below $\simeq 0.5\,M_\odot$ mass transfer is dynamically unstable for mass ratios $M_2/M_1 > 0.7$ (Webbink 1985). The lower limit of $0.38\,M_\odot$ for the mass of the secondary (Sect. 3.1) also does not fulfil the criterion for stability. Even if we assume an evolved secondary as in Kolb & Baraffe (1999) we arrive at masses of $0.31\,M_\odot$ for the white dwarf and $0.25\,M_\odot$ for the M star, again violating the stability criterion. The mass ratio is determined from the observed absorption line velocity and the inclination. So we turn the question around and ask, for which inclination would the stability criterion be satisfied? Taking the derived mass of the secondary we then need a primary mass of $0.64\,M_\odot$ and an inclination of 45.3°. That implies a variation of the viewing angle around this value, which in turn causes cyclotron emission lines to be shifted to the blue as compared to our data in Fig. 10. Especially above 8000 Å the spectral flux should strongly increase with wavelength for all phases due to the presence of the next lower harmonic, which in Fig. 10 only marginally shows up around phase zero. Therefore with our data we can see no remedy to the present situation. So the stability problem makes RX J1313.2–3259 an interesting system for future observations in four aspects: a) the contribution of the secondary star to the spectrum, best observable during a low state, b) the absorption line flux variation relevant for modelling the illumination, c) the degree of circular polarization as a function of orbital phase, and d) the white dwarf contribution to the spectrum, best observable in the ultraviolet regime.

Finally, we note that constraining the mass of the white dwarf is important for our understanding of the formation of cataclysmic variables, because with the period determined above models of common envelope evolution predict that the mass of the white dwarf should exceed $0.6\,M_\odot$ (de Kool 1992).

### *3.6. Mass accretion rates*

**Table 3.** Integrated fluxes from the accretion area and mass accretion rates. The units are $10^{-11}\,\mathrm{erg\,cm^{-2}s^{-1}}$ for the fluxes and $10^{-11}\,M_\odot\,\mathrm{yr}^{-1}$ for the mass accretion rates.

| | high state | low state |
|---|---|---|
| cyclotron emission | 1.7 | 0.2 |
| blackbody radiation | 1.0 — 3.0 | 0.0 — 0.1 |
| thermal bremsstrahlung | 0.1 — 0.3 | 0.1 |
| total flux | 2.8 — 5.0 | 0.3 — 0.4 |
| mass accretion rate | 4.3 — 7.7 | 0.5 — 0.6 |

For an estimate of the mass accretion rate one has to sum up all flux contributions from the accretion area. Although the optical and X-ray observations are not simultaneous we take the optical observations in Feb. 93 and the X-ray observations during the RASS as representative of the high state and those of Dec. 95 in the optical and July 92 in X-rays of the low state. To extend the observations to the whole frequency range we used the model fits for cyclotron emission, blackbody radiation, and thermal bremsstrahlung, respectively. The main uncertainty in these values is caused by the uncertainty in the blackbody temperature. Therefore we took the $1\sigma$ upper and lower limits of 68 and 41 eV (see Fig. 3) for the RASS data and assumed temperature limits of 15 and 50 eV for the PSPC data (see Sect. 3.4), to provide a range for the derived fluxes. The results are summarized in Table 3. From the total fluxes we computed the mass accretion rates for a distance of 200 pc, a white dwarf mass of 0.4 $M_\odot$, and a white dwarf radius of $1.08 \cdot 10^9$cm.

## 4. Conclusions

It has been shown that RX J1313.2–3259 belongs to the class of magnetic cataclysmic variables called AM Herculis binaries or Polars. It has a period of 251.4 min, which places it above the period gap, and a distance of $\simeq 200$ pc. From the occurrence of cyclotron humps a magnetic field strength of 56 MG for the main accreting pole has been deduced. The inclination is $i \simeq 66°$ implying a white dwarf mass of $\simeq 0.4$ $M_{\odot}$, with a likely mass for the secondary of 0.45 $M_{\odot}$, corresponding to a mass ratio $q \simeq 1.1$. A rough estimate of the mass accretion rate leads to $6{\cdot}10^{-11}$ $M_{\odot}\,yr^{-1}$ for the high state and $6{\cdot}10^{-12}$ $M_{\odot}\,yr^{-1}$ for the low state. The rather low mass of the white dwarf required for reproducing the observed cyclotron emission is in conflict with our present understanding of stable mass transfer and the evolutionary history of cataclysmic variables, so further observations of this system are of great interest.

*Acknowledgements.* The ROSAT project is supported by the Bundesministerium für Bildung und Forschung (BMBF/DLR) and the Max-Planck-Gesellschaft. We thank the ROSAT team at the MPE (Garching) for providing us with the results from the ROSAT All-Sky Survey and for their help with the data analysis. We also thank the staff at La Silla for competent assistence during the observations. This work has been supported in part by the DLR under grants 50 OR 9403 5 and 50 OR 9210 1.

## References

Baraffe I., Chabrier G., Allard F., Hauschild P.H., 1998, A&A 337, 403
Barrett P.E., Chanmugam G., 1985, ApJ 298, 743
Beuermann K., 1997, Magnetic cataclysmic variables: Observational and theoretical results. In: Agrawal P. (ed.), Perspectives of high-energy astronomy & astrophysics. Tata Institute of Fundamental Research, Mumbai, India
Beuermann K., Burwitz V., 1995, ASP Conf. Ser. 85, 99
Beuermann K., Thomas H.-C., 1990, A&A 230, 326
Beuermann K., Thomas H.-C., 1993, Adv. Space Res. 13 (12), 115
Beuermann K., Weichhold M., 1999, A&A (submitted)
Bessell M.S., 1979, PASP 91, 589
Campbell C.G., 1997, Magnetohydrodynamics in Binary Stars, Kluwer Acad. Publ., Dordrecht
Cropper M., 1990, Space Sci. Rev. 54, 195
de Kool M., 1992, A&A 261, 188
Gänsicke B.T., Beuermann K., de Martino D., 1999, A&A (in press)
Kolb U., Baraffe I., 1999, Secondary Stars in CVs: The Theoretical Perspective. In: Charles P.A., King A.R., O'Donoghue D. (eds.) Cataclysmic Variables: a 60th Birthday Symposium in Honour of Brian Warner. New Astronomy Reviews, Elsevier (in press)
Schwope A.D., 1995, Rev. Modern Astron. 8, p. 125
Thomas H.-C., Beuermann K., 1997, Proc. of IAU Coll. 166, Springer LNP 506, 247
Thomas H.-C., Beuermann K., Reinsch K., et al., 1998, A&A 335, 467
Voges W., Aschenbach B., Boller Th., et al., 1999, A&A 349, 389
Warner B., 1995, Cataclysmic Variable Stars, Cambridge Univ. Press, Cambridge
Watson M.G., 1994, ROSAT Results on Magnetic Cataclysmic Variables. In: Schlegel E.M., Petre R.(eds.) ROSAT Science Symposium. AIP Conf. Proc. 313, p.64
Webbink R.F., 1985, Stellar Evolution and Binaries. In: Pringle J.E., Wade R.A. (eds.) Interacting binary stars. Cambridge Univ. Press, Cambridge, p.39
Yentis D.J., Cruddace R.G., Gursky H., et al., 1992, The COSMOS/UKST Catalog of the Southern Sky. In: MacGillivray H.T., Thomson E.B. (eds.) Digitised Optical Sky Surveys. Kluwer, Dordrecht, p. 67
Zimmermann H.U., Becker W., Belloni T., et al., 1994, MPE report 257, Garching